# Analysing the sintering of heterogeneous powder structures by in situ microtomography

Luis Olmos, Didier Bouvard, Tetsu Takahashi, Christophe Martin, Luc Salvo, Daniel Bellet, Marco Di Michiel


# Analysing the sintering of heterogeneous powder structures by in situ microtomography

| | |
|---|---|
| Journal: | *Philosophical Magazine & Philosophical Magazine Letters* |
| Manuscript ID: | TPHM-09-Jan-0043.R2 |
| Journal Selection: | Philosophical Magazine |
| Date Submitted by the Author: | 22-Jun-2009 |
| Complete List of Authors: | Olmos, Luis; Grenoble INP, Laboratoire SIMAP<br>Bouvard, Didier; Grenoble INP, Laboratoire SIMAP<br>Takahashi, Tetsu; Grenoble INP, Laboratoire LMGP<br>Martin, Christophe; Grenoble INP, Laboratoire SIMAP<br>Salvo, Luc; Grenoble INP, Laboratoire<br>Bellet, Daniel; Grenoble INP, Laboratoire LMGP<br>Di Michiel, Marco; ESRF |
| Keywords: | composite materials, powder metallurgy, sintering |
| Keywords (user supplied): | X-ray microtomography, Porosity |
| | |

# Analysing the sintering of heterogeneous powder structures by in situ microtomography

Luis Olmos[(1)], Tetsu Takahashi[(1)], Didier Bouvard[(1)*], Christophe L. Martin[(1)], Luc Salvo[(1)], Daniel Bellet[(2)], Marco Di Michiel[(3)]

[(1)]Laboratoire SIMAP, Grenoble INP/CNRS/UJF, BP 46, 38402 Saint Martin d'Hères Cedex

[(2)]Laboratoire LMGP, Grenoble INP/CNRS, BP 257, 38013 Grenoble Cedex 01

[(3)]ESRF, BP 220, 38043 Grenoble Cedex, France

[*]Corresponding author



**Abstract**

This work analyzes the microstructure changes of various copper-based powder systems during sintering from 3D images provided by in-situ synchrotron microtomography. The investigated systems include a copper powder with a wide particle size distribution 0-63 µm poured into a quartz capillary, a presintered copper compact with artificially created large pores and a mixture of copper and alumina particles. The experiments were carried out at the European Synchrotron in Grenoble, France. Powders were sintered up to 1060°C under reducing atmosphere in a furnace located between the X-ray source and the detector. During each experiment, 3D images were taken at various times of the thermal cycle. We have obtained images with a resolution of 1.5 microns and the time of acquisition of every image was about one minute. Quantitative analysis of these images allowed the changes of various important parameters to be followed. Such parameters characterize the sintering process at the particle length scale: interparticle coordination, pore size distribution and particle centre to centre distance. Moreover, by tracking the displacement of each particle centre and comparing it to the displacement predicted by classical mean field assumption, we have been able to assess the magnitude of particle rearrangement occurring during sintering. From these data, the sintering behaviour of heterogeneous powder systems is discussed with particular emphasis of collective particle phenomena.

Deleted: is set of information

Keywords: Sintering, X ray microtomography, composites, porosity.

## 1. Introduction

In the last decades, progresses in understanding the physics of metal and ceramic powder sintering have been largely supported by the development of modelling, from prominent two sphere models [1-3] to more recent discrete element simulations [4,5]. Experimental investigations have not been as successful in capturing operative mechanisms because of the difficulty of directly observing the sintering process. Generally, sintered powders are observed post mortem by scanning electronic microscopy (SEM). With such a procedure, statistical data on the advancement of sintering can be obtained through the comparison of microstructural features at various points in the sintering cycle. However, following the alteration of an individual particle or of an individual pore during sintering is not possible. Additionally, the information directly provided by this technique is two-dimensional. Hence it is difficult to quantitatively investigate issues that are related to the collective behaviour of particles such as rearrangement and coordination evolution. The importance of particle rearrangement has been demonstrated early on by Petzow and Exner, who have measured particle rotations in 2D packing. [6].

X-ray microtomography now provides a non-destructive method to observe the microstructure of materials in 3D. This technique consists of recording radiographs of a specimen at various angular positions. The spatial distribution of the linear attenuation coefficient within the specimen is deduced from a mathematical algorithm. A 3D image of the microstructure is thus obtained when the phases composing the material have distinctive attenuation coefficients [7]. This is particularly convenient for powder materials where the pore phase is transparent to the X-rays. The use of the synchrotron radiation from third generation sources allows highly absorbing materials such as copper and iron to be characterized with a spatial resolution in the range from one to two micrometers [8]. Also, if the time of image recording is convenient, in situ observation of a material under mechanical or thermal loading is possible.

The first study of a sintered powder material by synchrotron microtomography has been performed by Bernard et al. [9] with glass beads sintering by viscous flow. These authors obtained 3D images of a specimen which sintering had been interrupted after various times. More recently, Lame et al. [10] and Vagnon et al. [11] achieved in situ characterization of the sintering of copper and steel metal powders with particle size of approximately 50 µm. After a

Deleted: directly

Deleted: times

Deleted: of

Deleted: a

Deleted: now

Deleted: in

Deleted: ie

Deleted: of the

quantitative analysis of the data obtained on copper powder [12], they found that sintering was quite homogeneous and that classical models based on mean field assumption agreed well with the experimental data. Nöthe et al. [13] confirmed the uniformity of sintering when he found limited amount of rotations of copper particles in 3D microtomography images taken at various stages of sintering. It should be pointed out that all of the aforementioned studies are concerned with quasi monosize, closely packed powders.

Deleted: above

The present paper presents results obtained by in situ synchrotron microtomography with more complex copper-based powder systems. These systems comprise particles with a broad size distribution and some of them include defects such as artificially created macropores or ceramic inclusions. One may anticipate a large effect of particle rearrangement for such systems with local heterogeneities. Novel tools have been developed for a more comprehensive analysis of 3D images, which involves in particular the evolution of interparticle contact indentation and the displacement of particle centres throughout sintering. The data drawn from this analysis allow discussion of the sintering behaviour of heterogeneous powder systems with particular emphasis on collective phenomena.

Deleted: discussing

## 2. Experimental procedure and image processing

Microtomography experiments were carried out at the European Synchrotron Radiation Facilities (ESRF) in Grenoble, France. Because copper is a material with a high absorption coefficient, it has been necessary to use high energy X-ray, which has been provided by ID15 beamline of ESRF. At ID15, the incoming X ray energy ranges between 35 and 90 keV after the filter. In the present experiments, a 50 keV energy was used. More details on the set-up can be found elsewhere [10, 11, 14]. The experimental set up allows the sample to be translated and rotated by 180°. A specialized furnace has been built at ESRF for sintering. This furnace is composed of a horizontal ceramic cylinder surrounded by a resistive wire. Three holes, one at the bottom of the furnace to allow for the introduction of the sample and two on both sides for the beam passage are located on the ceramic cylinder. Images were obtained with a 1 micron thick europium-doped Lutetium Aluminium Garnet (LAG) single crystal scintillator screen located in front of the detector system. The images provided by the scintillator were magnified 9 times with a microscope objective and recorded by a 1024 x 1024 CCD Frelon camera. The CCD camera has the following characteristics: a pixel size of 1.4 µm, and a full image readout time of 200 ms per image. 650 radiographs were recorded at

Deleted: specific

Deleted: ie

various angular positions covering an interval of 180° for each data set, which led to the capture of one microtomography data set in about one minute. With such an experimental set up, images with 1.6 µm sized voxels have been obtained.

Three samples have been investigated: a close packed copper powder, a copper-based powder composite and a copper powder compact with artificial pores. The atomised spherical copper powder was sifted to retain only particles smaller than 63 µm (Figure 1a) and then poured into a quartz capillary with 1 mm internal diameter and approximately 1 cm height. This capillary was pasted to an alumina rod attached to the positioning system. The second sample was composed of slightly sintered copper particles with artificially created pores. The procedure to create these large pores consisted of mixing the copper powder with 15% volume fraction of NaCl salt particles of 40 - 63 µm diameter. This mixture was then pre-sintered at 500°C for 30 minutes in a 1 mm diameter capillary, which was removed after cooling. The salt was finally dissolved by keeping the samples in distilled water during 5 hours. The resulting sample is displayed in Figure 1b. The sample was introduced in a quartz capillary for subsequent sintering. The third type of sample, the composite sample, was made of copper particles mixed with 16% volume fraction of spherical porous alumina particles (Figure 1c) with a diameter between 40 and 60 µm. These particles were mixed for one hour in a turbula and then poured in the same type of capillary as the one used for copper powder. The volume fraction has been selected based on the results of a previous study on the densification of various copper-alumina powder mixtures by dilatometry and scanning electron microscopy [15]. This prior study showed that the reduction of the densification rate due to the presence of alumina inclusions was already significant with 5 vol.% inclusions and was particularly drastic when the inclusion content was above 20%. Indeed, significant clustering of inclusions was observed for alumina content above 15%.

Sintering for all three types of sample was carried out at 1050°C after heating at 40 K/min under a reducing atmosphere (helium - 5 at.% hydrogen) to prevent oxidation of copper particles. The duration of the sintering plateau was different for the three samples. Because of the thermal expansion of the powder and of its swelling at intermediate temperature [16], the sample translated with respect to the X-ray beam during the observation. Thus, a slice of only 600x600x300 voxels could be tracked all along the thermal cycle.

Deleted: in
Deleted: during
Deleted: during
Deleted: by accounting for
Deleted: with various compositions
Deleted: It has been shown in t
Deleted: regard

3D raw images were treated in order to separate the phases by thresholding. The separation of pore and copper phases was straightforward and provided binary images of regular and porous copper samples. Concerning the composite material, alumina particles and porosity can hardly be distinguished by eye and not at all by automatic processing because the grey levels of alumina particles and porosity are very close. Hence, for this sample, we have prepared binary images where alumina inclusions and porosity appear as the same phase. This is unfortunate since it prevents the investigation of interesting phenomena such as inclusion coordination and clustering. Still, useful information concerning evolution of copper particles, which constitute the "active" phase of the composite material, has been drawn from binary images, as demonstrated in the following.

Deleted: with the

Deleted: originating from

Copper particle segmentation was achieved by a watershed procedure applied on binary images (for more details refer to Vagnon et al. [12]). The volume and the centre of gravity of each particle were then calculated from the segmented images. Contact indentation was defined as the relative displacement of particle centres. We evaluated the diameter of each particle as the diameter of an equivalent sphere with the same volume. Because of the presence of defects on the images (ring artefacts in particular) and of computer memory capacity, only ~500 particles have been followed during the whole sintering cycle. We present in Figure 2 an example of 2D images (virtual slices) extracted from 3D images showing the same microstructure after reconstruction, binarisation and segmentation. The segmentation procedure has proved more to be more problematic for increasing densities since particle interfaces become less clear. The upper acceptable limit was found to be around 0.75 in relative density. Such a limit is certainly higher in a monosize packing since the size of every particle to be separated is known.

Deleted: approximately

Deleted:

Deleted: only

Deleted: delicate

Deleted: are getting

Deleted: discernable

## 3. Results

### *3.1. General observations*

Figure 3 shows 2D images (virtual slices) of the microstructure inside every sample before and after sintering. Copper particle are easily discernible in the initial state but not so easily in the final stage. The quartz cylindrical capillary can be seen in the images. Regular and composite samples are initially in contact with the capillary because the powders have been directly poured into it. Conversely, the porous sample is smaller than the capillary because it

has been presintered before being introduced in the capillary. The radial shrinkage of each sample after sintering is clearly observed. The shrinkage of the composite sample is much smaller than the shrinkage of the other samples. Two types of pores appear in the porous sample: regular pores resulting from particle packing, as in the regular samples, and larger pores created by salt particle elimination. The regular pores exhibit a large decrease in size during sintering whereas the changes of the large pores are less significant. As mentioned above, the alumina particles can hardly be distinguished from the pores in the composite sample. Consequently, the alumina particles are incorporated in the porous phase in the following calculations. Obviously, these "filled pores" cannot shrink as the large pores of the porous sample.

Deleted: against

Table I shows various data for every specimen: the initial relative density, $D_0$, the relative density after the heating stage, the final relative density, $D_f$, the final densification ratio, defined as $(D_f-D_0)/ D_0$, the initial and final average particle sizes (averaged by number), the initial and final coordination numbers, $Z_0$ and $Z_f$. The relative density is defined as the weight density of the sample divided by the weight density of pure copper. The average particle size is initially between 33 and 42 µm, depending on the sample. It increases slightly during sintering due to the disappearance of the smallest particles. The initial densities of the regular and of the composite samples are equal because copper and alumina particles have approximately the same size. The initial density of the porous sample is 14% lower than the initial density of the regular sample. The final densification ratio for the regular sample is 0.24, sligthly larger for the porous sample (0.31), and much lower for the composite sample (0.1).

*3.2. Coordination number*

As expected, the initial coordination number is lower for the porous material than for the regular one (5.9 vs. 6.8). It is even lower in the composite material (5.6) because only copper-copper contacts are accounted for. It is worth noting that multiplying the initial coordination number of the regular sample by the volume fraction of copper particles in the composite sample leads to a coordination number of 5.7, which is very close to the one calculated for the composite material. To compare the coordination number evolution in the three materials, we have plotted in Figure 4 the coordination number versus the relative density, both normalized

by their initial values. Interestingly, all points lie close to a straight line of slope 1 which means that the coordination number is well approximated by the very simple relation:

$$Z = Z_0 \frac{D}{D_0} \tag{1}$$

It is shown in Figure 4 that this expression does not agree with the classical relation obtained by Arzt [17] from the assumption that the coordination number varies in accordance with the Radial Distribution Function (RDF) characterizing particle packing :

$$Z = Z_0 + 15.5\left(\left(\frac{D}{D_0}\right)^{1/3} - 1\right) \tag{2}$$

Arzt's relation significantly underestimates the increase in coordination found in microtomography specimens.

*3.3. Pore size distribution*

The pore size distribution is an important marker of the progress of sintering, especially so for heterogeneous systems such as those studied here. It should be pointed out that the porosity in such materials is completely open. It means that the pores cannot be considered as distinct elements and that the definition of a pore size distribution is somewhat ambiguous. Anyway, following Matheron [18], such a distribution can be estimated by measuring the porous volume accessible to a structural element of increasing size. For this purpose, we chose an octahedra of edge 3.2 µm (twice the voxel size) and multiples of this. Figure 5 shows the pore size distribution obtained in this way at various times during the sintering cycle for each of the three samples. The volume fraction corresponding to a given size interval is calculated as the volume inaccessible to the octahedron of the larger size of the interval minus the volume fraction accessible to the lower size. Each volume fraction is normalized by the total volume of the particles, which is constant throughout sintering. Using this measure, the global pore volume decrease related with densification is clearly detected. In the regular sample (Figure 5a), pore size is initially between 0 and 40 µm and most pores have a size around 11 µm. During sintering, the volume of the largest pores decreases and eventually pores between 30

Deleted: of

and 40 µm disappear. However the 11 µm pore size remains the most represented size in the distribution. Note that most of the pore changes occur during the sintering plateau at 1050°C.

In the porous sample (Figure 5b), the pore size is initially between 0 and 70 µm. The distribution exhibits a peak at 11 µm, as in the previous case, but also shows a clear plateau between 30 µm and 50 µm, which corresponds to the artificially created pores. These large pores get slightly smaller during the cycle. Meanwhile, the volume fraction of regular pores decreases with a maximum again at 11 µm. The pore size distribution in the presintered sample before sintering is very close to the one at the beginning of the 1050°C plateau.

Deleted: comprised

Concerning the composite sample (Figure 5c), whatever the sintering time, the pore size distribution exhibits two clear peaks around 14 and 60 µm, respectively. The value of 14 µm is larger than the value of 11 µm found in the previous samples. This is because the average particle size was fortuitously larger in the composite sample. The second peak features single alumina particles and pairs of particles. A third peak, although of lesser extent, can also be detected close to 100 µm. It indicates the presence of a few triplets of alumina particles, which form volumes approximately twice as large as the volume of a single particle.

### *3.4. Interparticle indentation*

In classical analysis derived from two sphere models, densification occurs during sintering because contacting particles get closer to each other through various diffusion mechanisms such as grain boundary diffusion and volume diffusion. The relative displacement of the centres of the two particles in contact with each other is defined here as the interparticle indentation and is denoted as $h$. According to the two sphere models, for two contacting particles with the same radius, $R$, the normalized indentation, i.e. the local deformation, $h/2R$, is a power function of $R$, with a negative exponent depending of the predominant diffusion mechanism. For particles with different sizes, $R_p$ and $R_q$, Parhami et al. [19] have suggested that the relevant parameter to account for size effects is the equivalent radius defined as:

$$\hat{R} = 2\frac{R_p R_q}{R_p + R_q} \qquad (4)$$

This definition has also the advantage of being in line with the general contact theory for elasticity and plasticity [20]. The pertinence of this parameter has been checked by using the following procedure. For each pair of contacting particles, we have determined the local deformation as the indentation divided by the distance between particle centres, $d_0$. We have found large scattering in values of this parameter at any given time, likely due to local heterogeneities in particle shape and arrangement. We have thus calculated the average of the local deformation for pairs of particles with radii $R_p$ and $R_q$ for which the equivalent radius has a given value. We have chosen three values of equivalent radius: 14, 20 and 28 µm. For each value, at least 30 pairs of particles were tracked. Note that, for example, the 14 µm equivalent radius set includes a pair with particles of 9 and 27 µm radii as well as pairs with particles of the same radius, 14 µm.

The average local deformation for the three samples is plotted in Figure 6 as function of the actual densification ratio defined as $(D\text{-}D_0)/D_0$. The use of the densification ratio allows for a fair comparison of the different materials. In each case, the deformation increases with increasing densification. Also, as expected from sintering theory, the deformation is larger for lower equivalent radius whatever the sample is considered. However, the curves associated with each sample show clear differences. For regular and composite samples, the deformation is very low until a densification ratio of approximately 0.025 is reached. This corresponds to the heating stage. The deformation then regularly increases throughout densification. For the same equivalent radius, larger local deformation is observed in the composite sample as compared to the regular sample at a given densification ratio. For the porous presintered sample, the deformation first exhibits a steep increase followed by a more gradual increase. It is smaller than the deformation in regular and composite samples, except at low densification ratio. Standard deviation bars plotted in Figure 6 indicate that the data corresponding to each equivalent radius are clearly separated. This observation suggests that the equivalent radius is able to reveal the size effect in sintering deformation.

*3.5. Particle tracking*

We take advantage of the ability of X-ray tomography to track individual particles to gain knowledge on particle rearrangement during the whole thermal cycle. We can draw, for example, the trajectories of particle centres in the analysed volume. Since 3D lines are hardly discernible in a 2D plot, we show in Figure 7 the horizontal projections of the trajectories.

Deleted: a
Deleted: for
Deleted: to
Deleted: all along
Deleted: catch
Deleted: possibility

According to the mean field theory, which assumes that the shrinkage is uniform throughout the sample, particle trajectories should be radial and particle displacement should be proportional to the distance between the particle and the volume centre. Most experimental trajectories seem to follow this rule but it is interesting to note that some of them significantly deviate from the radial direction. This is particularly obvious in the porous sample where a few trajectories are perpendicular to the radial direction.

For a quantitative analysis of particle displacement, we have calculated two parameters for each particle:

- the "deviation angle", θ, defined as the angle between the displacement vector – going from the initial position of the particle centre to its position at a given sintering time - and the radial direction, between 0 and 180°;

- the "closing parameter", $\delta = \left| \frac{u_r}{u_a} - 1 \right|$, where $u_r$ is the radial component of the displacement vector and $u_a$ is the length of the displacement vector predicted by the mean field theory. When the particle gets closer to the volume centre, exactly as predicted by the mean field, δ is equal to 0.

As an example, Figure 8 shows the values of both parameters for 350 particles analyzed in the porous material at a density of 0.62 (densification ratio : 0.1). It is observed that 90% of the particles exhibit a deviation angle between 10° and 70° and a closing parameter smaller than 0.7. There is no clear correlation between both parameters except for their largest values. Indeed, any particle with a deviation angle larger than 90° shows a closing parameter larger than 1, since it moves backward ($u_r < 0$) instead of following the forward mean field displacement ($u_a > 0$). There are only five particles with a deviation angle above 90°.

The average values of δ and θ have been calculated at various sintering times to quantify the relative amount of rearrangement for each sample. These values are plotted vs. the densification ratio in Figure 9. We observe that δ and θ averages show first a steep increase followed by a continuous decrease. The curves corresponding to the regular and composite samples are very close to each other whereas those corresponding to the porous specimen are always above the other two, except in the low densification ratio domain. However, it is not relevant to compare the beginning of the curves since the porous material experienced a presintering step before its introduction in the microtomography experimental set up. δ and θ

averages tend towards constant values, respectively, 0.14 and 18° for the regular material; 0.2 and also 18° for the porous material. For the composite material the final densification ratio is rather small and there is no clear asymptotic value.

## 4. Discussion

Quantitative data drawn from microtomography experiments provide useful information for a better understanding of microstructure evolution of metal powders during sintering. The relevance of the most interesting results is discussed in the following.

First, we have found a simple linear relation that reasonably describes the increase of average coordination number in the three investigated samples as function of relative density. It is worth pointing out that the same relation is relevant for very different materials such as a close packing of particles, a packing with large pores and a composite packing. This linear relation may be justified by using Arzt's Eq. (2) with an undefined factor α replacing 15.5. Linearization of this equation for $D$ close to $D_0$ leads to :

$$Z = Z_0 + \frac{\alpha}{3}\frac{D - D_0}{D_0} \quad (4)$$

where α is a constant. Eq. (4) yields Eq. (1) for $\alpha = 3Z_0$, i.e. , $\alpha = 20.4$ for our regular material. Eq. (1) is thus formally close to Arzt's model when the slope characterizing the Radial Distribution Function is increased. Also, Eq. (1) gives some credence to the linear empirical equation of Helle et al. [21].

$$Z = 12D \quad (3)$$

With the values of $Z_0$ and $D_0$ obtained for the regular material, we obtain $Z = 10.5\ D$.

Next, we have measured the pore size distribution according to Matheron definition [18]. For the regular sample with close packed particles, this distribution shows a clear peak around 11 µm throughout densification. This indicates that, although the powder densifies and the total amount of porosity decreases, the majority of pores consistently exhibit an equivalent size, which is approximately 27% of the mean particle size (40 µm). It does not mean

Deleted: the

Deleted: ly

Deleted: fairly

Deleted: all along

however that 11 µm size pores are stable. All pores in the packing shrink but, as the largest pores shrink more slowly, the peak of the distribution remains the same. This trend has been observed for relative densities below 0.8. It is expected that the pore size decreases when the density approaches unity. In the other samples, a peak also appears in the distribution at approximately the same size value but a second population of much larger pores is also detected. In the porous sample, the size of the artificially created pores is in between 30 and 70 µm. These pores merely show a slight reduction in size during sintering. The analysis of composite sample data is not so pertinent since alumina inclusions have been lumped together with the porosity in the image analysis. We find once again that real pores exhibit a stable size, which is slightly larger than in the previous cases. Inclusion-filled pores also show evidence of a stable size of approximately 60 µm.

To analyse the indentation between particles of different sizes, an equivalent radius defined as the harmonic mean of both radii has been introduced. We have found that in average the normalized indentation – i.e. the local deformation - increases when the equivalent radius decreases. This means that the equivalent radius allows size effect in sintering to be taken into account in a simple manner. For the same densification ratio, in the porous sample, the local deformation is lower, whatever the value of the equivalent radius. This result demonstrates that the contribution of interparticle indentation to the densification is less important in the porous sample than in the regular one. In other words, a more significant part of the densification seems to come from particle rearrangement in the porous sample. In contrast, a larger indentation is required in the composite sample to reach a given densification ratio. This is clearly linked to the presence of non-deformable inclusions that impose copper particle to sinter more for the sample to attain a given macroscopic relative density.

The evaluation of particle rearrangement has been carried out by analysing the deviation of particle displacement with regard to the mean field theory. .For this purpose, we have defined two parameters, one to characterize the deviation from the radial direction and another one to characterize the radial component of the displacement. These parameters have been calculated for all particles in the investigated volumes and for each specimen. Average values of these parameters have been calculated for quantification of particle rearrangement. The analysis of the variations of both parameter averages prove that rearrangement mainly occurs at the beginning of the densification. However, the three materials show dissimilar behaviours. For the regular and the composite samples, rearrangement is most important during the heating

stage. This is because contact size, at this early stage of sintering, is very small and thus does not impede particle motions. Also, the packing density is still small enough at this stage to allow for particle rearrangement. For the porous material, which has been presintered, the rearrangement peak is observed later, after a few minutes at the temperature plateau. A reasonable interpretation is that this peak results from the conjunction of low packing density and high temperature. In any case, the values of average parameters at the end of the sintering plateau prove that rearrangement has been globally more important in the porous specimen in comparison with the regular and composite specimens. This last result is consistent with the indentation data described above, which showed that particle indentation was smaller in the porous material for a given densification ratio.

Deleted: commented

## 5. Conclusion

It has been shown that in situ X-ray microtomography was particularly appropriate for gathering data on collective particle behaviour during sintering. The wealth of information that this technique provides in 3D allows a better understanding of phenomena such as the evolution of multiple contact deformation or particle rearrangement. These phenomena play a significant role in sintering, and more particularly in heterogeneous powder systems as demonstrated here. The most relevant outcomes are :

- The estimate of a prominent pore size equal to 27% of the average particle size, which is constant at least up to 0,8 of relative density,
- the minor shrinkage of artificially introduced large pores,
- the linear relation between the coordination number and the relative density, for all samples, including the composite packing,
- the relevance of the defined equivalent radius to describe the sintering of pairs of particles with different sizes,
- the definition of two parameters related with particle displacement that allowed for a quantification of rearrangement,
- the conjunction of a slightly stronger rearrangement and a lower interparticle indentation in the porous material in comparison with the regular one at the same densification ratio.

The investigation methods presented in this paper are also useful for guiding the development of modelling techniques such as discrete element modelling [22]. They can provide both

information for building realistic numerical microstructures and data for validating the results of the models.

It should be remembered that this work has been restricted to the initial stage in sintering for two reasons. First, individual particles cannot be separated from 3D images when the relative density is larger than 0.75. Secondly, due to microtomography resolution, we have been compelled to sinter relatively coarse powders, which can hardly been densified above 85% relative density in a reasonable time. With a higher resolution in the future, we should be able to work with finer powders and then investigate denser structures, thus allowing the transition from open to close porosity together with the final stages of pore evolution to be analysed.

**References**


1. J. Frenkel, J. Phys. (Moscow), 9 (1945) p.385.
2. G.C. Kuczynski, Trans. Am. Inst. Min. Metall. Eng. **185** (1949) p.169.
3. Coble R.L., J. Am. Ceram. Soc. **41** (1958) p.55.
4. C.L. Martin, L.C.R. Schneider, L. Olmos and D. Bouvard, Scripta Mat. **55** (2006) p.425.
5. B. Henrich, A. Wonisch, T. Kraft, M. Moseler and H. Riedel, Acta Mater. **55** (2007) p.753.
6. G. Petzow and H. Exner, Z. Metallkd. **67** (1976) p. 279
7. A. C. Kak and Malcolm Slaney, *Principles of Computerized Tomographic Imaging*, IEEE Press, 1988.
8. D.H. Bilderback, P. Elleaume and E. Weckert, J. Phys. B: At. Mol. Opt. Phys. **38** (2005) p.S773.
9. D. Bernard, D. Gendron, J.M. Heintz, S. Bordére and J. Etourneau, Acta Mater. **53** (2004) p.121.
10. O. Lame, D. Bellet, M. Di Michiel and D. Bouvard, Acta Mater. **52** (2004) p.977.
11. A. Vagnon, O. Lame, D. Bouvard, M. Di Michiel, D. Bellet and G. Kapelski, Acta Mater. **54** (2006) p.513.
12. A. Vagnon, J.P. Rivière, J.M. Missiaen, D. Bellet, M. Di Michiel, C. Josserond and D. Bouvard, Acta Mater. **56** (2008) p.1084.
13. M. Nöthe, M. Schulze, R Grupp, B. Kieback, A. Haibel and J. Banhart, Mater. Sci. Forum. **534-36** (2007) p.493.

14. M. Di Michiel, J.M. Merino, D. Fernandez-Carreiras, P. Falus and T. Martins, Rev. Sci. Instrum. **76** (2005) p.043702.
15. L. Olmos, C.L. Martin and D. Bouvard, Powder Technol. **190** (2009) p.134.
16. A. Upadhyaya and R. M. German, Int. J. Powder Metall. **34** (1998) p.43.
17. E. Arzt, Acta Metal. et Mater. **30** (1982) p.1883.
18. G. Matheron, *Eléments pour une théorie des milieux poreux*, Masson, Paris, 1967
19. F. Parhami, R.M. McMeeking, A.C.F. Cocks and Z. Suo, Mech. Mater. **31** (1999) p.43.
20. K.L. Johnson, *Contact mechanics*, Cambridge University Press, Cambridge, 1985.
21. A.S. Helle, K.E. Easterling and M.F. Ashby, Acta Metall. **33** (1985) p. 163
22. L. Olmos, C.L. Martin, D. Bouvard, D. Bellet and M. Di Michiel, J. Am. Ceram. Soc. , to be published

**Table caption :**

Table I : Data characterizing the three samples.

**Figure caption**

Figure 1 : SEM observation of copper powder (a), presintered porous sample (b), alumina powder (c)

Figure 2 : Virtual slice of a regular copper sample (a) after reconstruction and (b) after binarisation and segmentation

Figure 3 : Virtual slices of samples in the initial state (left side) and after sintering (right side). (a) et (b) : regular sample; (c) and (d) : porous sample; (e) and (f) : composite sample

Figure 4 : Normalized coordination number vs. normalized relative density.

Figure 5 : Pore size distribution at various times of the sintering cycle for regular (a), porous (b) and composite (c) samples

Figure 6 : Average normalized particle indentation as function of the densification ratio for three values of equivalent radius, 14 , 20 and 28 µm, (a) regular, (b) porous and (c) composite.

Figure 7 : Planar projection of particle centre trajectories in the horizontal plane during sintering in regular (a), porous (b), composite (c) samples and schematic definition of displacement parameters (d)

Figure 8 : Distribution of the parameters characterizing particle rearrangement, the deviation angle θ and the closing parameter δ, in the porous specimen at a densification ratio of 0.1.

Figure 9 : Evolution of the average values of δ (a) and θ (b) during densification for the three samples.

| Material | Initial relative density, $D_0$ | Relative density after heating | Final relative density, $D_f$ | Densification ratio, $(D_f - D_0)/D_0$ |
|---|---|---|---|---|
| **Regular** | 0.645 | 0.665 | 0.800 | 0.24 |
| **Porous** | 0.563 | 0.57 | 0.735 | 0.31 |
| **Composite** | 0.650 | 0.673 | 0.713 | 0.10 |

| Material | Initial average particle size (µm) | Final average particle size (µm) | Initial coordination number, $Z_0$ | Final coordination number, $Z_f$ |
|---|---|---|---|---|
| **Regular** | 37 | 43 | 6.8 | 8.6 |
| **Porous** | 33 | 40 | 5.9 | 7.7 |
| **Composite** | 42 | 44 | 5.6 | 6 |

Table I : Data characterizing the three samples.

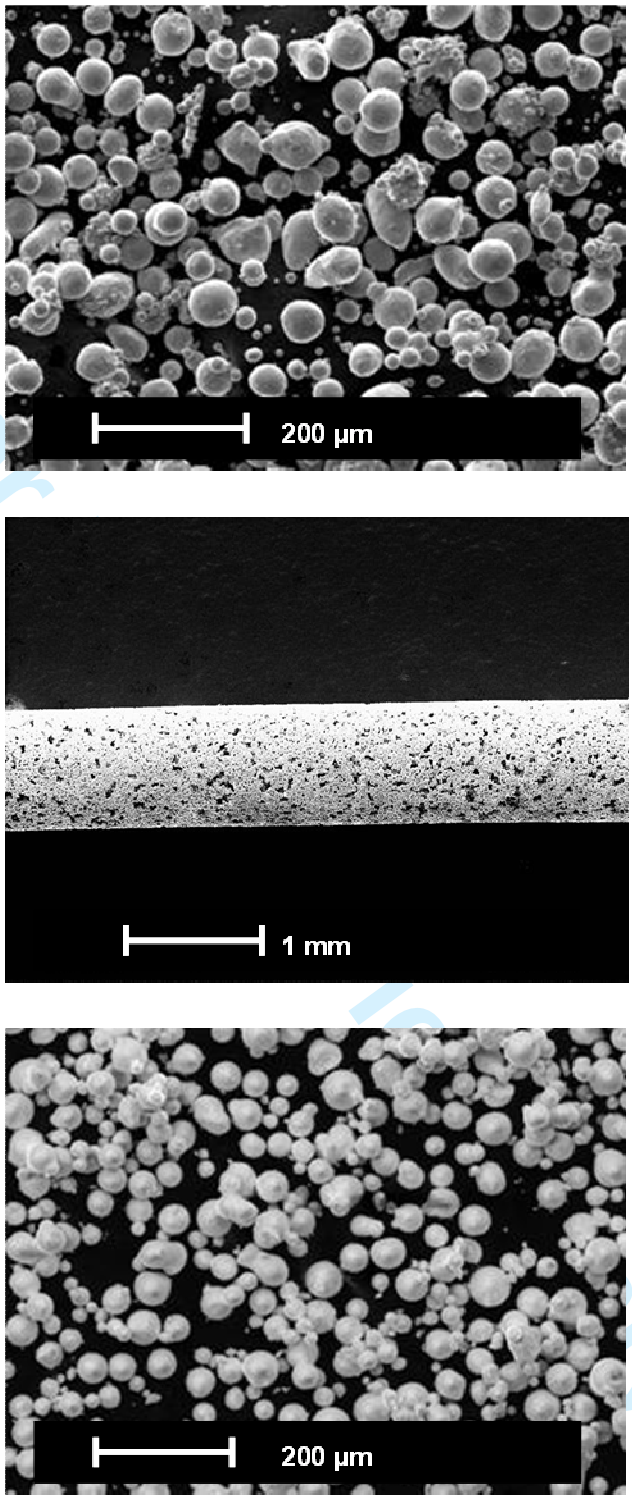


Figure 1

(a) 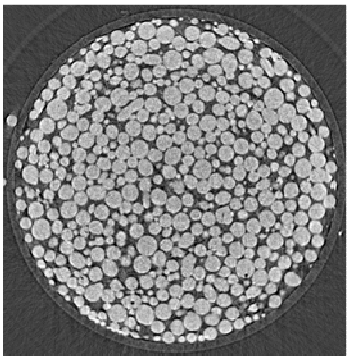 (b) 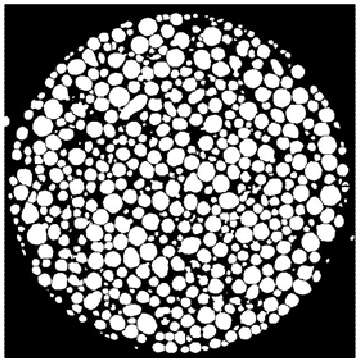

Figure 2

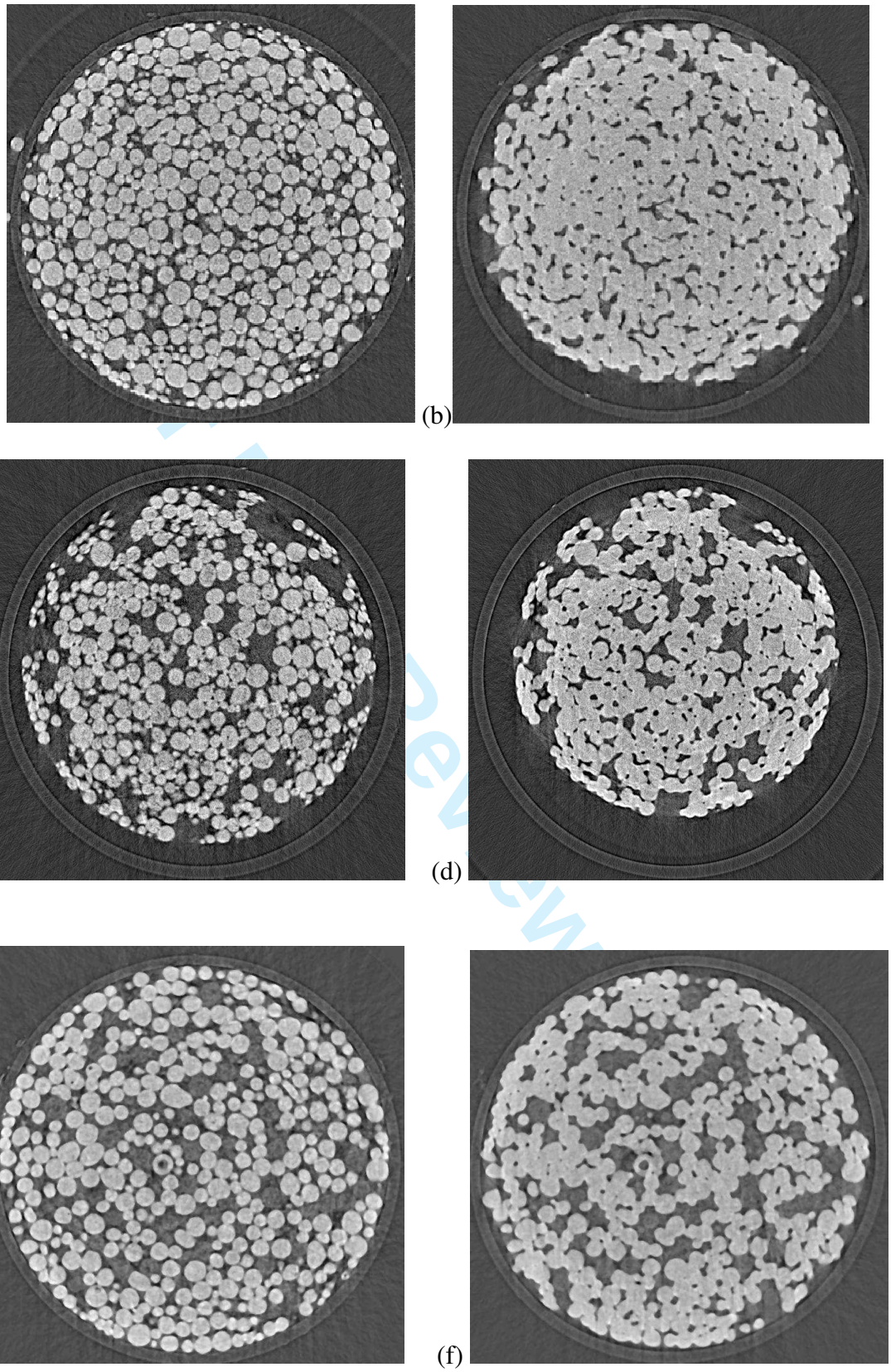


Figure 3

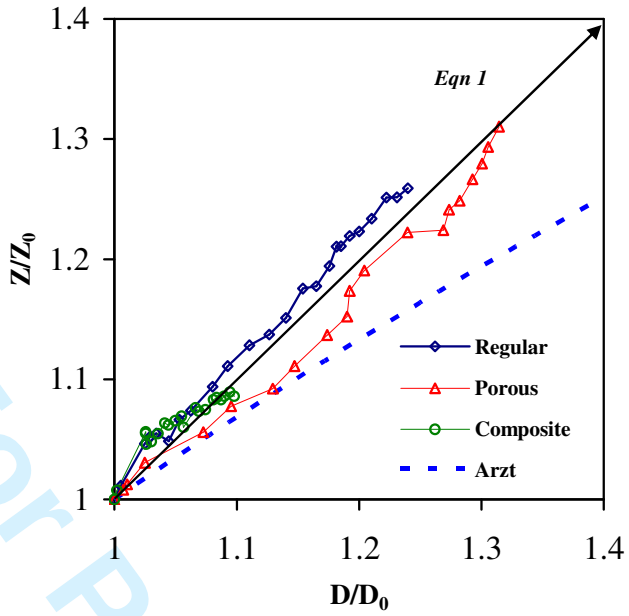


Figure 4

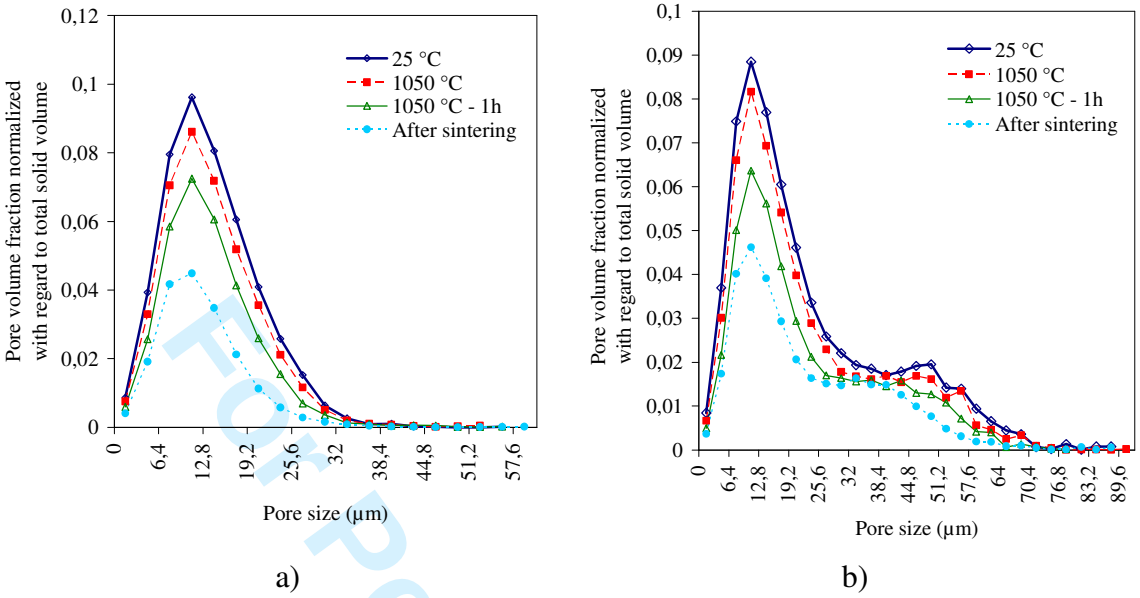


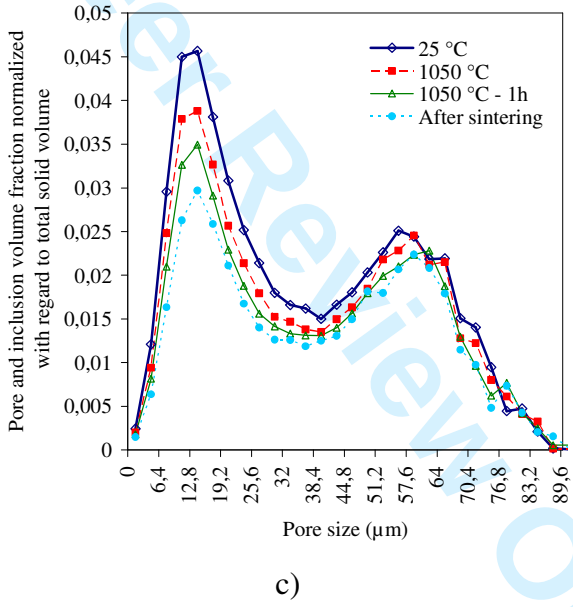


Figure 5

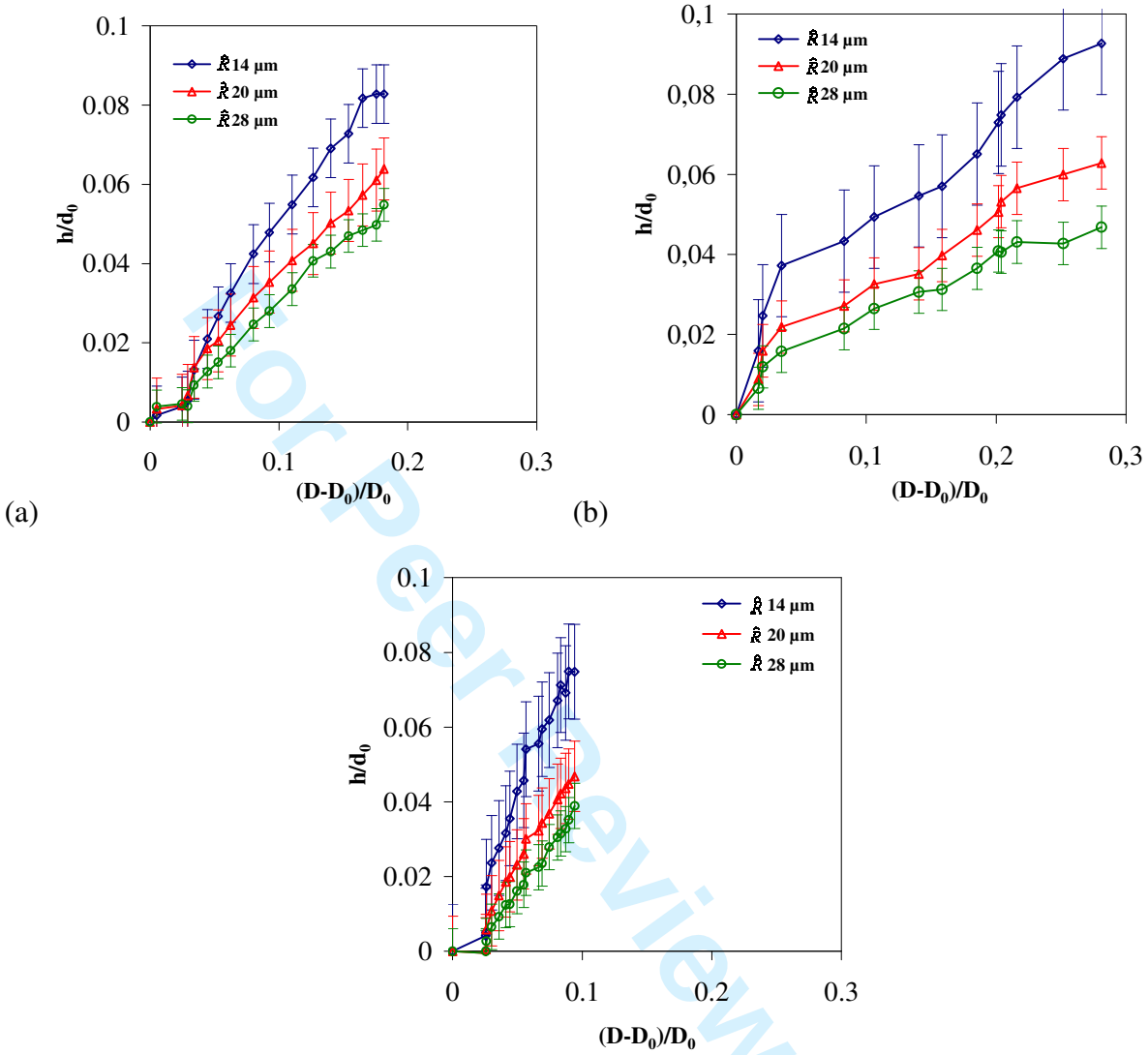


Figure 6

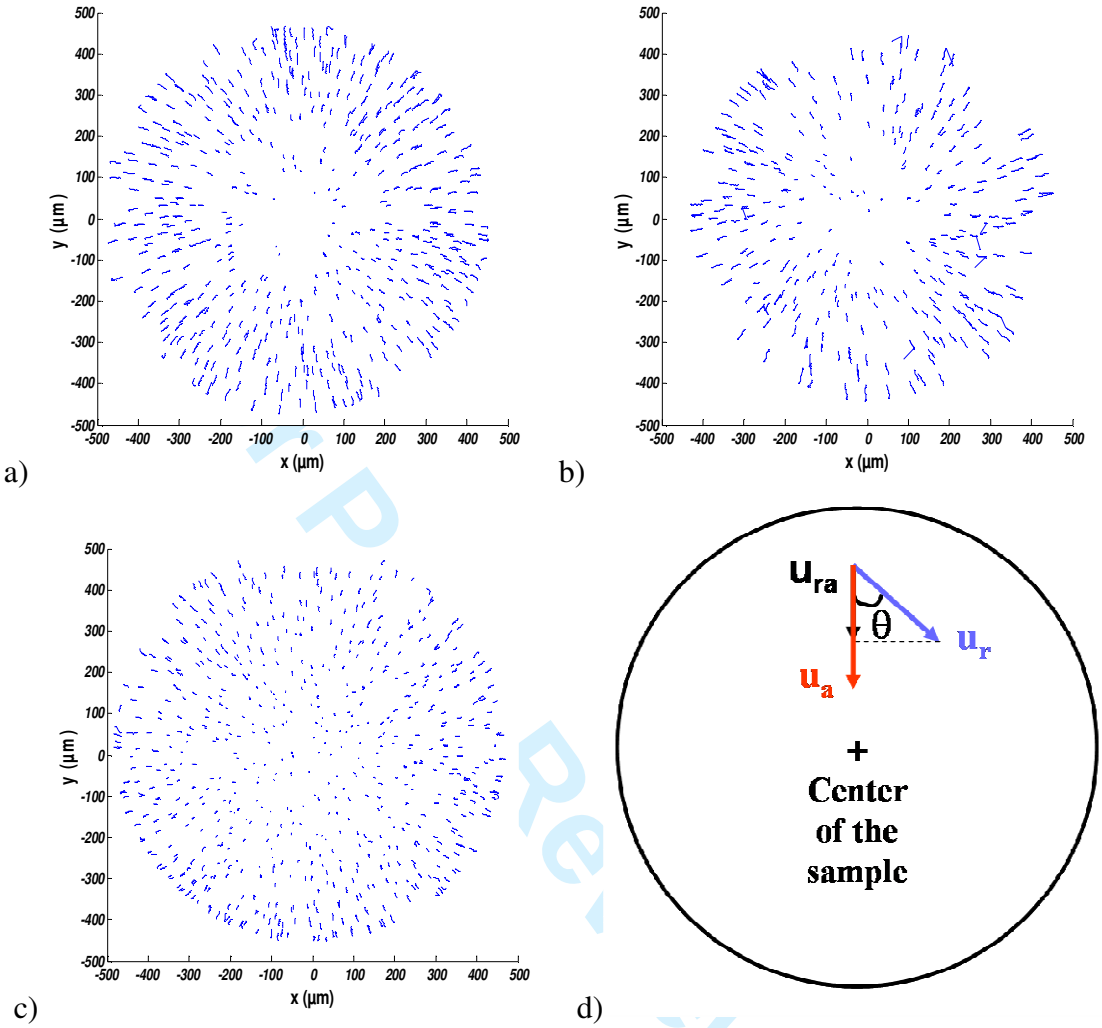


Figure 7

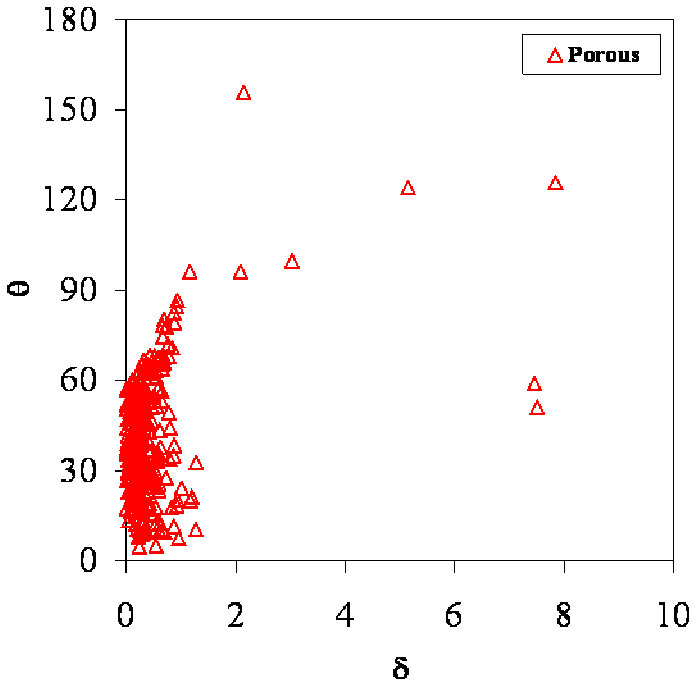


Figure 8

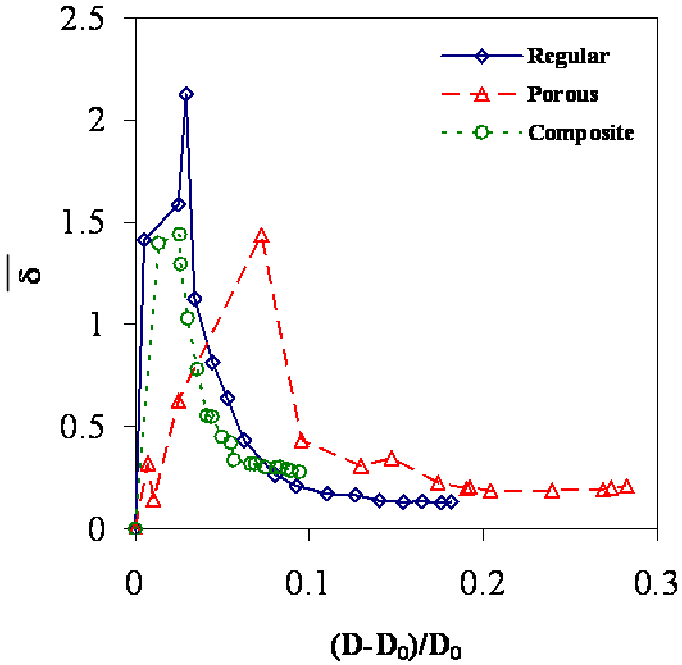
2.5
2
1.5
1
0.5
0
|δ
0
0.1
0.2
0.3
(D-D0)/D0
Regular
Porous
Composite

(a)

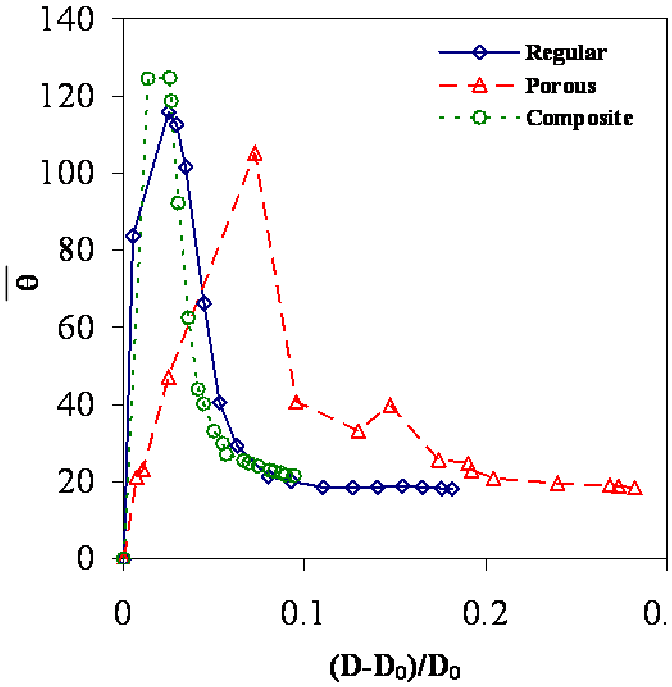
140
120
100
80
60
40
20
0
|θ
0
0.1
0.2
0.3
(D-D0)/D0
Regular
Porous
Composite

(b)

Figure 9